RESEARCH ARTICLE

Open Access

Spin-orbit-locked hyperbolic polariton vortices carrying reconfigurable topological charges

Mingsong Wang[1†], Guangwei Hu[1,2†], Saroj Chand[1], Michele Cotrufo[1], Yohannes Abate[3], Kenji Watanabe[4], Takashi Taniguchi[5], Gabriele Grosso[1,6], Cheng-Wei Qiu[2] and Andrea Alù[1,6*]

Abstract

The topological features of optical vortices have been opening opportunities for free-space and on-chip photonic technologies, e.g., for multiplexed optical communications and robust information transport. In a parallel but disjoint effort, polar anisotropic van der Waals nanomaterials supporting hyperbolic phonon polaritons (HP^2s) have been leveraged to drastically boost light-matter interactions. So far HP^2 studies have been mainly focusing on the control of their amplitude and scale features. Here we report the generation and observation of mid-infrared hyperbolic polariton vortices (HP^2Vs) associated with reconfigurable topological charges. Spiral-shaped gold disks coated with a flake of hexagonal boron nitride are exploited to tailor spin–orbit interactions and realise deeply subwavelength HP^2Vs. The complex interplay between excitation spin, spiral geometry and HP^2 dispersion enables robust reconfigurability of the associated topological charges. Our results reveal unique opportunities to extend the application of HP^2s into topological photonics, quantum information processing by integrating these phenomena with single-photon emitters, robust on-chip optical applications, sensing and nanoparticle manipulation.

Keywords: Hyperbolic polariton vortex, Light-matter interactions, Spin-orbit interaction, Topological charge, Reconfigurability

1 Introduction

Low-dimensional materials form an emerging platform for exotic light-matter interactions, ideally suited for various photonic technologies [1–5]. In these materials, light hybridizes with matter to form quasiparticles known as polaritons [6, 7], which feature deeply subwavelength field confinement and broadband responses spanning from terahertz to infrared and visible frequencies. The hyperbolicity of polaritons supported by various natural materials, especially in anisotropic van der Waals

(vdW) crystals, is particularly promising for next-generation nanophotonics. The hyperbolicity originates from extreme anisotropy of the atomic interaction between in-plane covalent and out-of-plane vdW bondings [8], enabling unusually large wave momenta associated with giant field confinement and slow group velocities over broad bandwidths. While hyperbolic phenomena have been originally explored in engineered metamaterials, such as metal–insulator-metal multilayers, this approach suffers from inevitable fabrication imperfections and finite granularity, resulting in enhanced loss and nonlocality hindering their widespread applicability [9, 10]. Natural hyperbolic polaritons in polar vdW crystals [11] can overcome these challenges: for instance, hexagonal boron nitride (hBN) conical nanoresonators enable remarkably large quality-factors (~ 283) and light confinement ($\sim \lambda/86$) [12]. In addition, the dispersion

---

[†]Mingsong Wang and Guangwei Hu contributed equally to this work

*Correspondence: aalu@gc.cuny.edu

[1] Photonics Initiative, Advanced Science Research Center, City University of New York, New York City, NY 10031, USA
Full list of author information is available at the end of the article

of hyperbolic phonon polaritons (HP^2) can be engineered with large flexibility, as shown in hBN [12–17] and α-MoO$_3$ [18–23], facilitating super-resolution imaging [14, 15], light canalization [17, 20], molecular sensing [24, 25], reconfigurable propagation [26, 27], for a variety of polaritonic applications [11, 28].

So far, the manipulation of hyperbolic phonon polaritons (HP^2) has been mainly limited to amplitude control, while adding new degrees of freedom may dramatically expand the impact of polaritonics for information processing and transport. For instance, surface plasmon polaritons (SPPs) have recently been explored to control phase, spin and orbit angular momentum (OAM) as independent degrees of freedom [29–35]. Based on these principles, a plasmonic vortex has been explored to enhance the channel capacity of on-chip optical communication networks [36]. Plasmonic OAMs can selectively couple to the spin of light excitation, inducing spin–orbit interactions [37, 38] and spin-controlled plasmonic phenomena, such as unidirectional routing [39], plasmonic vortex generation [29, 30, 40, 41] and information detection, opening new opportunities for low-energy information processing and computing. Extending these explorations to the polaritonic regime in the mid-IR range is exciting on various fronts: (1) we can expect significantly reduced loss compared to their plasmonic counterparts; (2) mid-IR frequencies are of particular interest for on-chip communications and sensing, since several biomolecules have fingerprints in this range; (3) endowing phonon polaritons with these new degrees of freedom unlocks new forms of low-energy information transport and processing. Low-dimensional phonon-polariton nanomaterials offer an ideal playground to enable this vision. The lack of exploration of HP^2 in the context of phase and angular momentum control may be associated with the fact that most polaritonic materials support bulk polariton modes, in contrast with plasmon polaritons that travel at interfaces, making more difficult the excitation, observation, and direct access to these phenomena.

2 Results and discussion

In this paper, we tackle and address these challenges by coupling HP^{2}s to tailored nanostructures, leveraging refined theoretical design and observing the response via real-space near-field nanoimaging. Specifically, we demonstrate infrared nanoscale HP^2 vortices (HP^{2}Vs) induced in pristine hBN thin flakes (Fig. 1a), associated with highly reconfigurable topological charges emerging at the HP^{2}V center. Our system is composed of a gold (Au) disk with Archimedean spiral shape used to launch HP^2 in hBN. We first study spin–orbit interactions in this system, revealing unprecedented control of HP^2,

the precise generation of nanoscale vortices with associated topological charges locked to the excitation spin. Based on scattering-type scanning near-field microscopy (s-SNOM) [13, 16, 42, 43], HP^{2}Vs are observed in real space, and spin–orbit control and tunability are accordingly demonstrated. Our results reveal new degrees of freedom and enhanced robustness in HP^2 control based on optical spin–orbit interactions and topological charges, ideally suited for super-resolution sensing and imaging, enhanced light-matter interactions, communications and multiplexing, and particle manipulation [44] at mid-IR frequencies.

As schematically illustrated in Fig. 1a, our sample is composed of a thin hBN flake transferred onto a shaped Au disk. The edge of the nanodisk acts as an HP^2 launcher, tailored to convert incident free-space light into strongly confined near fields at the disk boundary, resulting in efficient launching of HP^{2}s [14, 15]. hBN flakes are known to support discrete waveguide modes based on bulk HP^{2}s [13], denoted by the mode index s associated with their in-plane momentum of $k_{t,s}$, t refers to the axis parallel to the hBN flake. Unlike free-space beams or SPPs, HP^2 propagation is characterized by a large wavevector k confined to the angle $\theta = \arctan\left(\sqrt{-\frac{\varepsilon_t}{\varepsilon_z}}\right)$ with respect to the optical z axis, i.e., the axis perpendicular to the hBN flake, as illustrated in Additional file 1: Fig. S1. ε_z and ε_t are the hBN permittivity components along the z axis and in the orthogonal plane, respectively. Polariton fringes are expected to form with periodicity $\delta_r = 2d\tan\theta$ on the top hBN surface, where d is the flake thickness.

In order to generate a polariton vortex in hBN, we control the optical path of the launched hyperbolic polaritons by tailoring the disk shape to follow an Archimedean spiral, $r_{AS}(\phi) = r_{min} + \frac{\mathrm{mod}(m\phi, 2\pi)}{2\pi} * g$, where g indicates the rate of increase of the spiral radius with the azimuthal angle ϕ, and the integer parameter m denotes the number of spiral arms. As an example, a Au disk with outer shape mapping a four-arm spiral was fabricated, and its atomic force microscope (AFM) image is shown in Fig. 1b, where r_{max} and r_{min} are the maximum and minimum radius and $g \equiv r_{max} - r_{min}$. Based on this design, the polaritons induced on the top surface are expected to support a phase distribution as a function of position (r,ϕ) in the $z = z_0$ plane following

$$\varphi(r, \phi, z_0) = k_{t,s}\left(r_{AS}(\phi) - r_{min} + \frac{\delta_r}{2}\right) + s'2\pi \qquad (1)$$

where $s' \equiv s - 1$ is the modified HP^2 order on the flake with a Au substrate (see Sect. 4). As experimentally verified in Fig. 1, the induced HP^{2}s indeed follow spiral orbitals in space to form a vortex with topological features. In
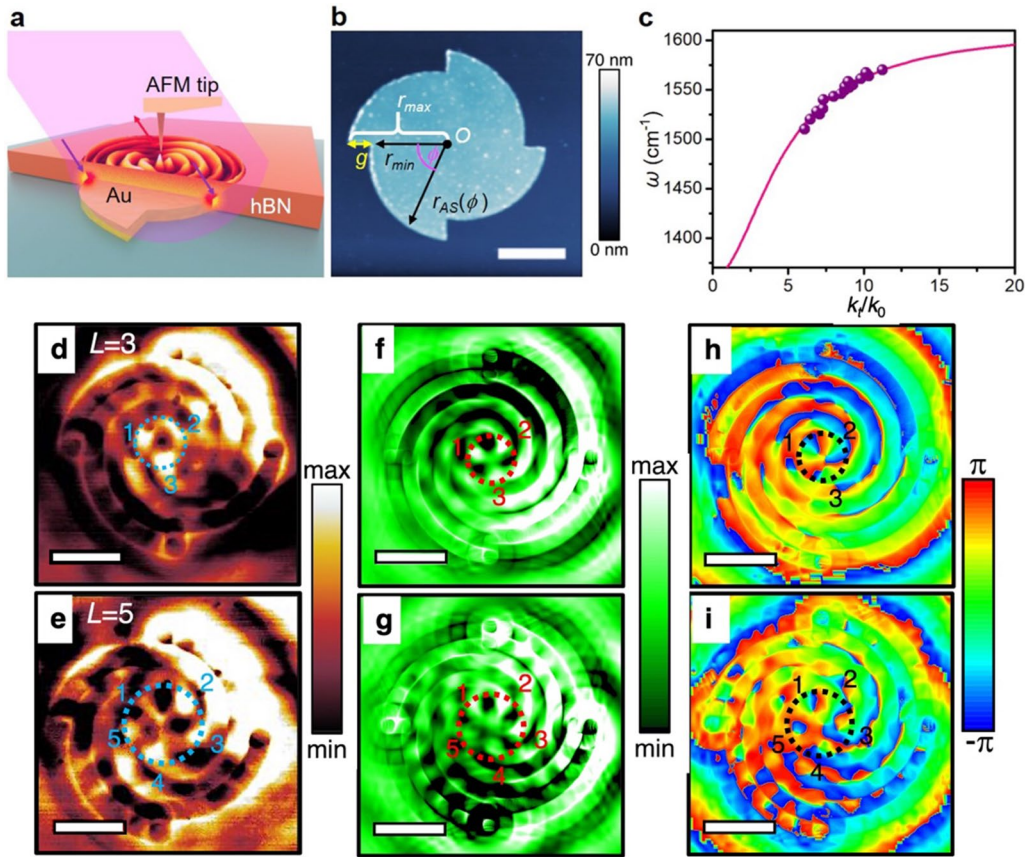
Fig. 1 Polariton vortex, dispersion, simulation and experimental results for an hBN flake excited through an Au spiral disk with $m = 4$. **a** Schematic of the geometry and experimental setup. **b** AFM image of Au disk shaped as a left-handed Archimedean spiral with four arms, r_{max} and r_{min} are the maximum and minimum radii, g is their difference, φ is the azimuthal angle and $r_{AS}(\varphi)$ is the distance from the center (O). **c** Dispersion of k_t for the sample in panel b. Purple spheres and pink curve are experimental and calculated results, respectively. **d**–**i** Near-field amplitude images at ~ 1546 cm^{-1} (**d** and **e**), simulated E_z (**f** and **g**), and phase (**h** and **i**) distributions at ~ 1546 cm^{-1}. Top and bottom images are obtained under RCP and LCP light illumination, respectively. The black dotted circle in the phase images indicates the spiral phase. The scale bar is 2 μm in all panels

particular, if the Archimedean spiral shape satisfies the condition

$$k_{t,s}\left(g + \frac{\delta_r}{2}\right) = l2\pi, \tag{2}$$

the phase accumulation from $\phi = 0$ to $\phi = 2\pi$ is $m(l + s') * 2\pi$ for an Archimedean spiral with m arms. The integer l is the orbital topological charge supported by the induced HP^2 spatial distribution.

Under a circularly polarized plane wave excitation, due to spin–orbit interactions in the near-field, the total phase accumulation is $(l * m + \sigma)2\pi$, associated with a topological charge of total angular momentum

$$L = m(l + s') + \sigma, \tag{3}$$

where $\sigma = +1$ or -1 or left-handed (LCP) or right-handed circularly polarized (RCP) incident light, as we

assumed a left-handed spiral. Equation 3 outlines the several degrees of freedom available to control our HP^{2}Vs, as a result of the complex interplay between incident spin and geometry-induced control of the polariton orbitals. Nontrivial control parameters consist of the spiral geometry (e.g., g), the working frequency (i.e., $k_{t,s}$ and l when g is fixed), the number of spiral arms m, the excited polaritonic mode s', and the excitation spin σ. In our demonstration, we focus on the dominant mode, $s' = 0$.

HP^{2}Vs carrying a discrete topological charge L are expected to support a spiral phase accumulation of $L*2\pi$ and a phase singularity at their center [45], controlled by the spin of impinging light [29, 46–48]. As described by the previous analysis, this spin-dependent phase originates from spin-to-orbital angular momentum conversion enabled by the coupling between the spin angular momentum (SAM) of the excitation and the OAM [37].
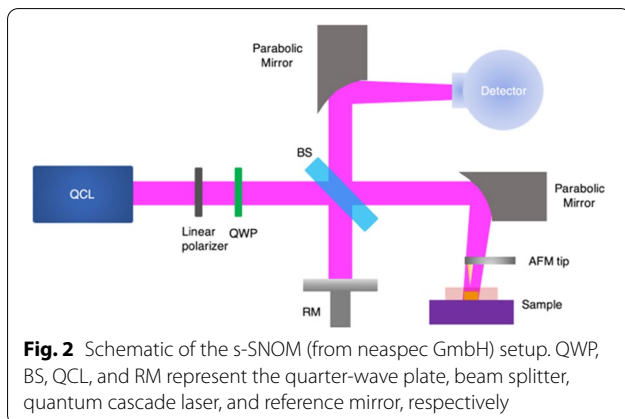
To observe HP²Vs and the associated spin–orbit interactions in real space, we used s-SNOM measurements to map HP²s on the top surface of a hBN flake in Fig. 1a. The setup of our experiment is schematically shown in Fig. 2: we fabricated a Au four-arm Archimedean spiral disk over a SiO_2 top layer on a silicon substrate, shown in Fig. 1b, with $g = 650$ nm, $r_{min} = 2.275$ μm and height $h = 65$ nm (details in Methods). Consistent with the previous analysis, the parameter h and r_{min} do not affect the total topological charge induced in the HP²V. An exfoliated hBN flake with a thickness of ~ 295 nm was transferred on top of the Au disk. By acquiring multiple near-field images with excitation frequency spanning from 1510 to 1570 cm^{-1} (see examples in Additional file 1: Fig. S2), we retrieved (Fig. 1c) the in-plane momentum (k_t) of the fundamental HP² mode at different frequencies, which agrees well with the analytical dispersion calculated based on the parameters in ref. [13].

Figure 1d, e show the measured near-field distribution of polariton fringes at ~ 1546 cm^{-1}, yielding a clear spiral shape profile emerging from the interference of HP² fields launched by the disk boundary with the incident field at the tip. At this frequency, $\lambda_t \approx 761 nm = \lambda_0/8.5$, where λ_t and λ_0 are the in-plane and free-space wavelength, respectively, confirming a deeply subwavelength confinement of the induced HP²V. The simulated electric field ($|E_z|$) profile shown in Fig. 1f, g matches well with experimental results (see more details in Methods). Consistent with Eq. 3, when $l = 1$ a left-handed spiral with $m = 4$ yields polariton vortices with topological charge $L = 3$ and $L = 5$ for LCP and RCP excitation, respectively. By comparing Fig. 1d, e (or Fig. 1f, g), we notice a distinct difference in induced field profile at the vortex center, associated with the different topological charge. Both experimental and simulation results reveal that HP²V with $L = 3$ has a smaller ring-shaped profile at its center than $L = 5$, when l is fixed. This is expected, since

its size increases with the spiral phase, consistent with other optical and plasmonic vortex studies [29, 45, 49]. Our setup imprints this dynamic into nanoscale phonon polaritons. It should be mentioned that the regions of the dotted circles in Fig. 1f–i and below figures are determined by the spiral phase at the center in near-field phase images and their positions are chosen to have a minimum deviation from their center to that of the Au patterns. The calculated phase distributions at ~ 1546 cm^{-1} under RCP and LCP excitation, shown in Fig. 1h ($L = 3$) and Fig. 1i ($L = 5$), reveal clockwise 3*2π and 5*2π spiral phase variations at the origin, further confirming the nature of spin–orbit interactions for $\sigma = +1$ and -1. The discrete topological charge associated with these polariton vortices introduces inherent robustness to geometric perturbations associated with topological features [50], and new degrees of freedom for polaritonic science and technology.

Next, we experimentally demonstrate precise reconfigurability of HP²Vs, besides the incident spin demonstrated in Fig. 1. According to Eq. 3, both orbit topological charge (l) and the Archimedean spiral geometry (m) control the total induced angular momentum of the polariton vortex. Here, l is controlled by the frequency of impinging light when g and d are fixed, following the polariton dispersion. In Fig. 3, using geometric arguments we predict the phase accumulation ϕ_{PP} along the azimuthal angle ϕ for $m = 1, 2, 4$ when $l = 1, 2$, revealing a broad range of opportunities in terms of polariton field profiles and induced topological charges that can be generated using this platform. In these plots, we do not explicitly take into account the additional degree of freedom stemming from the excitation spin, which enables an additional knob for manipulation. Because a large L leads to more dramatic amplitude and phase variations, and higher-order HP²Vs correspond to sharper field profiles, which are more difficult to image [30], in the following we demonstrate this broad reconfigurability for $m = 1, 2$ and $l = 1, 2$.

We first explore the near-field profile of the induced HP²Vs and their dependence on the number of Archimedean spiral arms m. Figure 3b, c show AFM images of Au disks with one- and two-arm Archimedean spirals, i.e., $m = 1, 2$, respectively. The parameters g, r_{min}, and h are the same as in the previous examples, and a thinner exfoliated hBN flake with $d \sim 170$ nm was transferred on top of the Au disks. Our experimentally measured polariton dispersion (see examples of amplitude images in Additional file 1: Fig. S3) agrees well with the analytical one also for this flake (Fig. 3d), showing larger transverse wavevectors, i.e., more confined polariton fields, compared to the results in Fig. 1c, due to the thinner nature of this flake. As seen in Eq. 2, larger wavevectors enable
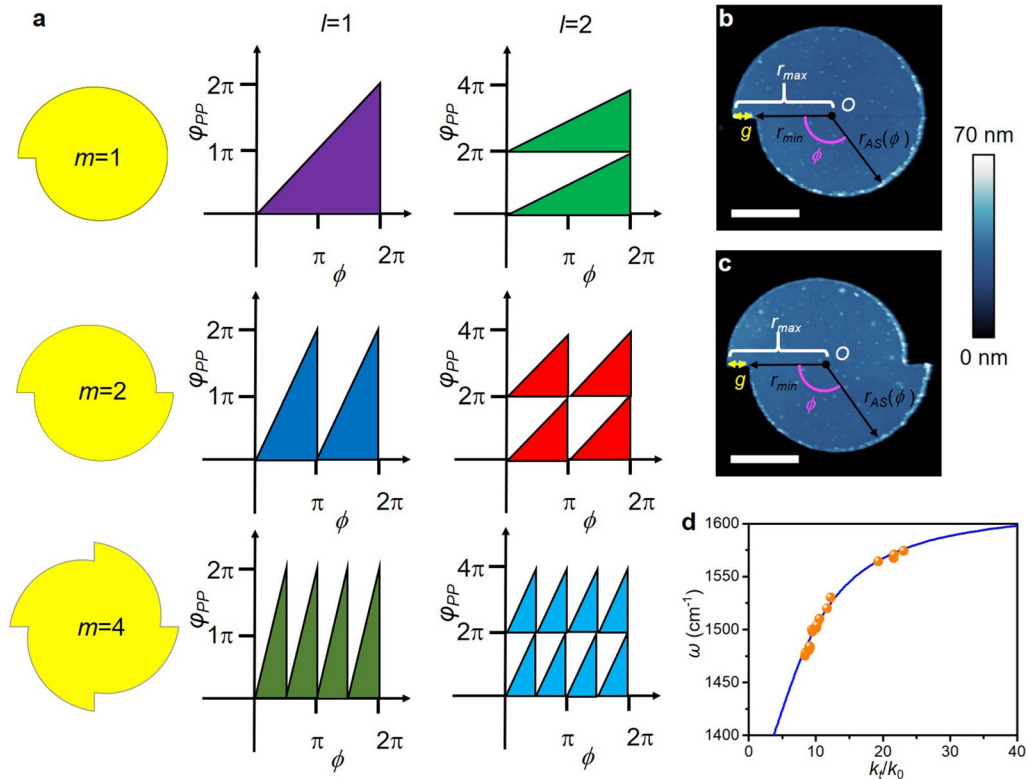

Fig. 2 Schematic of the s-SNOM (from neaspec GmbH) setup. QWP, BS, QCL, and RM represent the quarter-wave plate, beam splitter, quantum cascade laser, and reference mirror, respectively

Fig. 3 Polariton vortex phase accumulation vs azimuthal angle for $m=1$, 2 and 4 when $l=1$ and 2, and Au disk images and k_t dispersion for polaritonic vortices with $m=1$, 2. **a**, φ_{PP} and φ denote the accumulated phase and azimuthal angle, respectively. **b,c** AFM images of Au disk with one (**b**) and two (**c**) left-handed Archimedean spiral arms. **d** Dispersion of k_t for samples in (**b,c**). Orange dots and navy curve are experimental and calculated results, respectively

access to larger l for fixed g, hence supporting vortices with $l=1$ and $l=2$ around 1542 cm^{-1} and 1561 cm^{-1}. Based on Eq. 3, for $l=1$ we expect $L=0$ (1) when $m=1$ (2) under RCP light excitation, and $L=2$ (3) when $m=1$ (2) for LCP light.

The corresponding near-field images, showcasing the wide reconfigurability of polariton vortices enabled by these structures, are shown in Fig. 4. For $L=0$, the phase distribution around the HP^{2}V center is uniform, supporting a subwavelength polariton focal spot, rather than a ring profile as expected for nonzero topological charges (Fig. 4a). Figure 4e shows the corresponding numerical simulations, showing a good agreement. By varying the number of spiral arms or the excitation SAM, we can reconfigure the topological charge L. For example, increasing m from 1 to 2 makes L increase from 0 to 1, resulting in a different size of the central spot, which becomes ring-shaped and grows larger, as seen comparing Fig. 4a, g (Fig. 4c, i for simulations). Further growth of the central ring profile is obtained under LCP illumination (Fig. 4b and h), as this SAM yields larger values of L, again confirmed by our numerical simulations (Fig. 4d,

j). It should be noticed that as revealed by the associated spiral phase in Fig. 4f the upper bright lobe close to the central amplitude profile in Fig. 4d is not a part of the central pattern while at an outer layer of the spiral pattern, so L is 2 not 3 in Fig. 4d. As L increases, we also verify that the polariton vortex phase accumulation grows in discrete 2π steps, as illustrated in Fig. 4e, f, k, l. We find 0 to $3*2\pi$ spiral phase accumulation around the center, confirming a discrete growth of topological charge L from 0 to 3. These images also show a $2*2\pi$ phase difference between LCP and RCP excitation, demonstrating strong spin–orbit polariton interactions.

Extreme HP^{2}V reconfigurability can also be achieved by controlling the orbital topological charge l, which can be tuned through the excitation frequency. Figure 5 shows results with a similar trend as in Fig. 4 retrieved from the same samples at ~1561 cm^{-1}, for which the increased k_t of the supported polaritons yields an orbital topological charge $l=2$. As a result, the total angular momentum of HP^{2}V correspondingly increases compared to the $l=1$ scenario. Since HP^{2}s support a broad range of frequency-dependent k_t thanks to their hyperbolic dispersion [11,
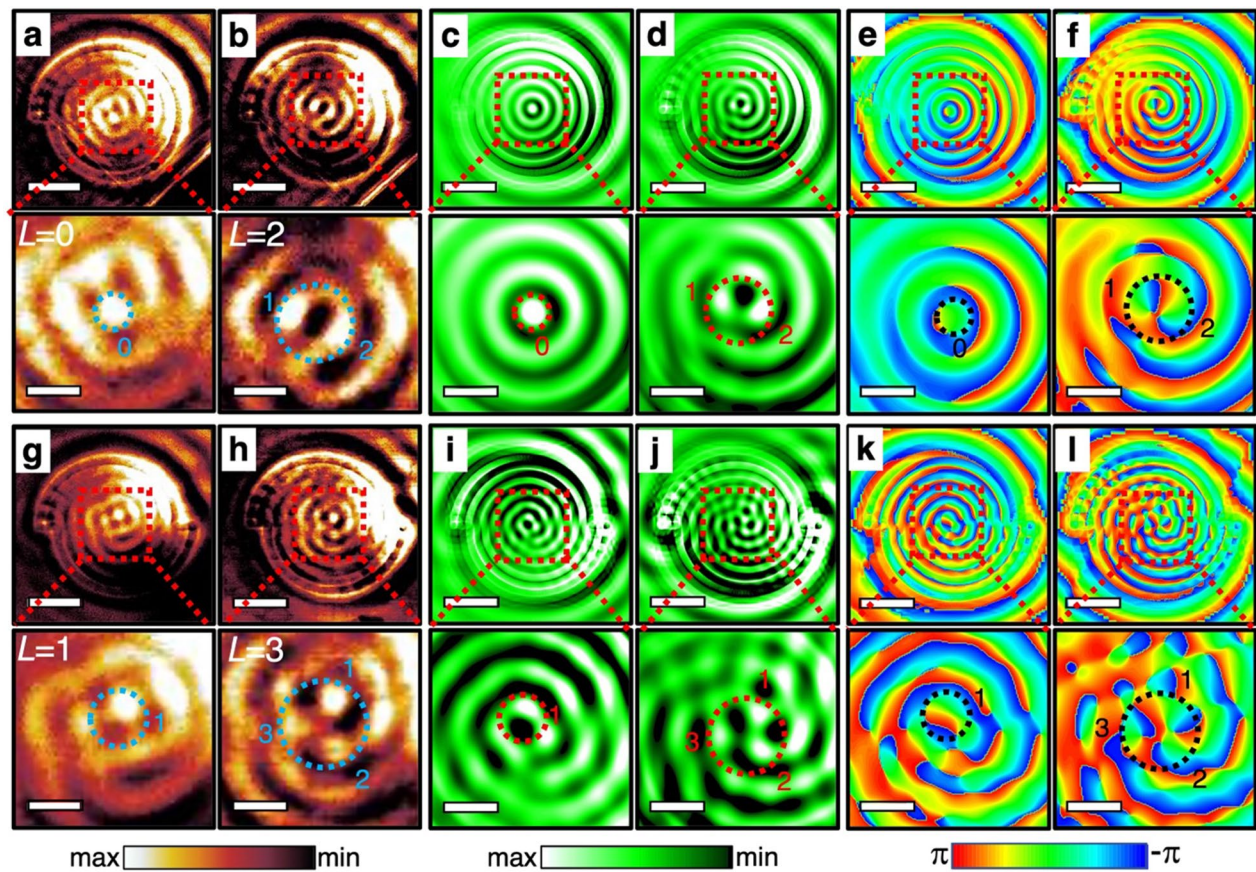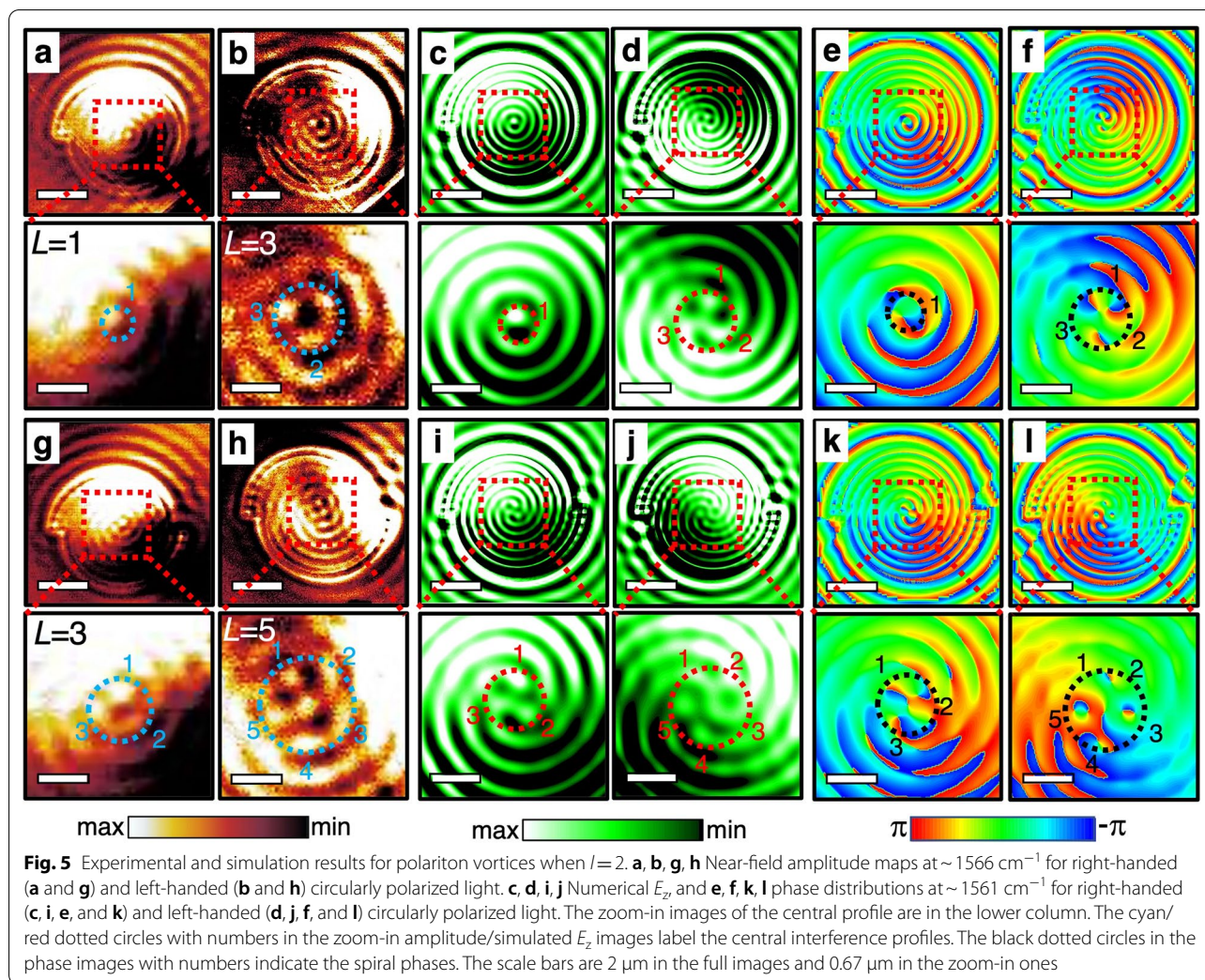
Fig. 4 Experimental and simulation results for polariton vortices when $l = 1$. **a**, **b**, **g**, **h** Near-field amplitude images at ~ 1550 cm^{-1} for right-handed (**a** and **g**) and left-handed (**b** and **h**) circularly polarized light. **c**, **d**, **i**, **j** Numerical E_z and **e**, **f**, **k**, **l** phase distributions at ~ 1542 cm^{-1} for right-handed (**c**, **i**, **e**, and **k**) and left-handed (**d**, **j**, **f**, and **l**) circularly polarized light. The zoom-in images of the central profile are in the lower column. The cyan/red dotted circles with numbers in the zoom-in amplitude/simulated E_z images label the central interference profiles. The black dotted circles in the phase images with numbers indicate the spiral phases. The scale bars are 2 μm in the full images and 0.67 μm in the zoom-in ones

13], a wide range of l can be attained, enabling broad reconfigurability of HP^{2}Vs without varying the sample geometry. The demonstrated nano-vortices have deeply subwavelength spatial profile, again supported by the extreme HP^2 field confinement. A comparison between experimental and simulated images in Figs. 4 and 5 shows that even denser fringes are obtained when $l = 2$, consistent with the larger k_t and shorter polariton wavelength (Eq. 1) combined with increased topological charge. At ~ 1550 cm^{-1} (Fig. 4a, b, g, h), $\lambda_t \approx \lambda_0/14.8$ ($l = 1$), while at ~ 1566 cm^{-1} (Fig. 5a, b, g, h) $\lambda_t \approx \lambda_0/19.5$ ($l = 2$). The near-field profiles at the vortex center are supported through the superposition of HP^{2}s excited from the Au disk boundary, so we can expect that the size of the HP^{2}V central profile narrows as l increases. To further explore how the phase profile evolves with l, we compare Fig. 4h, j, and l ($l = 1$) with Fig. 5g, i, and k ($l = 2$). A sharper phase variation and a smaller central profile can indeed be observed at the higher frequency, despite the fact that

in both scenarios the induced topological charge is the same ($L = 3$). For the $L = 5$ scenario when $l = 2$ in Fig. 5l the spiral phase is less well defined compared to the one in Fig. 1i, associated with the fact that the spiral phase is less stable at larger L when $l = 2$ than $l = 1$. Overall, Fig. 5 features HP^{2}s with very large transverse momentum, realizing polariton vortices with highly confined features, offering unprecedented opportunities for super-resolution mid-IR imaging, high-precision particle manipulation, sensing, and high-density information storage and transmission. When l is larger than 2 the associated frequencies become too close to the 1610 cm^{-1}, i.e., the high-frequency edge of the upper Reststrahlen band of [13]. Therefore, it is not possible to obtain a clean central profile in this scenario, because of increased loss and reduced group velocity of the associated polaritons (more discussions can be found in the Additional file 1).

During the review of this study, Xiong et al. reported topological spin textures of phonon polaritons by

Fig. 5 Experimental and simulation results for polariton vortices when $l = 2$. **a, b, g, h** Near-field amplitude maps at ~ 1566 cm^{-1} for right-handed (**a** and **g**) and left-handed (**b** and **h**) circularly polarized light. **c, d, i, j** Numerical E_z, and **e, f, k, l** phase distributions at ~ 1561 cm^{-1} for right-handed (**c, i, e,** and **k**) and left-handed (**d, j, f,** and **l**) circularly polarized light. The zoom-in images of the central profile are in the lower column. The cyan/red dotted circles with numbers in the zoom-in amplitude/simulated E_z images label the central interference profiles. The black dotted circles in the phase images with numbers indicate the spiral phases. The scale bars are 2 μm in the full images and 0.67 μm in the zoom-in ones

illuminating a ring-shaped antenna located on top of an hBN flake with circularly polarized light [51]. In their study, meron-like textures with a half-integer topological charge, determined by the handedness of the incident circularly polarized light, were observed, linking transverse SAM to skyrmion/meron-like textures in polaritons [51–53]. Here, we explore the spin–orbit interaction between OAM and out-of-plane SAM and the control of total topological charges via multiple degrees of freedom.

3 Conclusions
Overall, in this work we have conclusively demonstrated spin–orbit locked HP^2Vs emerging in natural polar vdW crystal hBN flakes coupled to spiral structures with tailored in-plane chirality. The resulting devices generate broadly reconfigurable topological charges, showcasing exotic polaritonic features, including spin–orbit

interactions and nanofocusing. The demonstrated polariton vortices are highly tunable using various degrees of freedom, including the excitation spin, the geometry of the polariton launcher, and the hyperbolic features of the underlying material controlled by the wavelength of excitation. Our demonstration of HP^2V opens unique opportunities to robustly process multiplexed information at mid-IR wavelengths and has great potential for super-resolution imaging systems with multiplexing capabilities, ultracompact mid-IR sensors, and miniaturized polaritonic devices with robust features associated with their topological nature, as well as enhanced nonlinearities and sensing. Overall, our findings broadly enrich the nanophotonic and polaritonic platforms enabled by vdW nanomaterials with phase, spin, and orbital angular momentum engineering capabilities, of great interest for a variety of classical and quantum applications.

4 Methods

4.1 Sample preparations

Gold (Au) disks with Archimedean spiral shapes were prepared through standard electron beam lithography (EBL). EBL resist (PMMA) was first spin-coated on a silicon dioxide (SiO_2) layer on a silicon substrate, and the desired patterns were created by exciting the resist with the electron beam. After resist developing in an MIBK-IPA solution, a 65-nm-thick Au layer was deposited on top of the sample via electron beam evaporation, and the resist was lifted off. Atomic force microscope (AFM) images of the realised Au disks are shown in Figs. 1b and 3b, c. Hexagonal boron nitride (hBN) flakes were obtained through mechanical exfoliation of high-quality hBN crystals. hBN flakes were transferred on top of the Au disks via a dry transfer method, as shown in Additional file 1: Fig. S4.

4.2 Near-field measurements

A commercial scattering-type scanning near-field optical microscope (s-SNOM) (neaspec GmbH) was used to record the near-field images of the hyperbolic polaritonic vortex (HP^{2}V) in hBN. A quantum cascade laser (QCL) with tunable wavelength (MIRcat-QT by DRS Daylight Solutions) was employed as the mid-infrared light source. The s-SNOM measurement was based on a tapping-mode AFM, and a commercial AFM tip with PtIr$_5$ coating (NanoWorld) was utilized to probe the local near field on the top of the hBN flakes. The scattering signals from the tip were recorded by a pseudo-heterodyne interferometric detection module with AFM tapping amplitude of $\sim$70 nm at a fixed wavelength. The obtained signals were demodulated at the 2$^\text{nd}$ harmonic of the oscillation frequency, which is about 285 kHz. A schematic presentation of the setup is shown in Fig. 2.

As shown in Fig. 2, a circularly polarized mid-IR beam was produced by passing a linearly polarized beam through a mid-IR quarter-wave plate, and then focused on the sample with a parabolic mirror. In order to verify whether the beam focused by a parabolic mirror still preserves circular polarization, we compared the output intensities of two setups: with and without a parabolic mirror, as schematically illustrated in Additional file 1: Fig. S5. The results obtained at 1510 cm^{-1} are listed in Additional file 1: Tables S1 and 2, which prove the preservation of circular polarization after the beam is focused by the parabolic mirror. An Au disk without spiral arms covered by an hBN flake was then measured to confirm that HP^2 with $\sigma = +1$ and -1 can be excited under LCP and RCP incident light, respectively. The results are shown in Additional file 1: Fig. S7 and are in good agreement with the simulations. In addition, Additional

file 1: Fig. S8 unveils that there are important differences between the amplitude images retrieved under linearly and circularly polarized light. Please see more discussions in Additional file 1.

4.3 Theoretical analysis and numerical simulations

For a hBN thin layer on top of a perfect electric conductor (PEC) substrate, the phonon polariton (PhP) mode in hBN can be obtained by finding the poles of the dyadic Green's function, which is equivalent to the transverse resonance condition:

$$2k_{z,s}d + \angle R_1 + \angle R_2 = s2\pi, \; s = 0, 1, 2, \ldots \quad (4)$$

where d is the thickness of hBN, $R_1 = -\frac{\varepsilon_1 k_z - \varepsilon_t k_{z1}}{\varepsilon_1 k_z + \varepsilon_t k_{z1}}$ and $R_2 = \frac{\varepsilon_2 k_z - \varepsilon_t k_{z2}}{\varepsilon_2 k_z + \varepsilon_t k_{z2}}$ are the reflection coefficient at the top surface and bottom surface; The top and bottom material are assumed to have permittivity ε_1 and ε_2, respectively. Here, $k_{z1} = \sqrt{\varepsilon_1 k_0^2 - k_t^2}$; $k_{z2} = \sqrt{\varepsilon_2 k_0^2 - k_t^2}$; and $k_{z,s} = \sqrt{\varepsilon_t k_0^2 - \frac{\varepsilon_t}{\varepsilon_z} k_t^2}$, where k_t is the in-plane wavevector and the index s denotes the s-th waveguide mode. For large wavevector, we have:

$$k_{z,s} \approx k_{t,s}\sqrt{-\frac{\varepsilon_t}{\varepsilon_z}} = k_{t,s}\tan\theta \quad (5)$$

i.e., $k_{t,s} = \frac{k_{z,s}}{\tan\theta}$, where θ is the angle with respect to the optical axis (z axis) for a Type II hyperbolic band. A fringe at the top surface can be formed with evolving periodicity $\delta_r \equiv 2d\tan\theta$. Alternatively, Eq. (4) can be written as

$$k_{t,s} = -\frac{\Psi}{d}\left[\arctan\left(\frac{\varepsilon_1}{\varepsilon_t}\Psi\right) + \arctan\left(\frac{\varepsilon_2}{\varepsilon_t}\Psi\right) + s\pi\right]$$

where $\Psi \equiv \frac{\sqrt{\varepsilon_z}}{i\sqrt{\varepsilon_t}}$. If the substrate is gold at mid-infrared frequency, $\text{Re}[\varepsilon_2]<0$ and $|\varepsilon_2| \gg 0$, we thus have $\arctan\left(\frac{\varepsilon_2}{\varepsilon_t}\Psi\right) \to -\frac{\pi}{2}$ and $|R_2| \to 1$ while $\angle R_2 \to -2\pi$. Therefore, the lowest-order mode is $s=1$. This differs from the case of dielectric substrates with positive permittivity. Nevertheless, one can rewrite this mode as

$$k_{t,s} = -\frac{\Psi}{d}\left[\arctan\left(\frac{\varepsilon_1}{\varepsilon_t}\Psi\right) + (s-1)\pi\right]$$
$$= -\frac{\Psi}{d}\left[\arctan\left(\frac{\varepsilon_1}{\varepsilon_t}\Psi\right) + s'\pi\right]$$

where we defined $s' \equiv s - 1$ for brevity. In order to form a vortex, we design the Au disk to have an Archimedean spiral shape, which can be mathematically written as $r_{AS}(\phi) = r_0 + m\frac{\text{mod}(\phi, 2\pi)}{2\pi}g$, where r_0 is the minimum value of the radius and g is a geometric parameter indicating the rate of increase of the radius with the

azimuthal angle ϕ, defined as $g = r_{AS}(\phi = 2\pi) - r_0$. The integer parameter m denotes the number of consecutive Archimedean arms in the pattern. We can calculate the phase of the polariton distribution at the top surface, given by the evolution of the polaritons launched from the edge:

$$\varphi(r,\phi) = k_{t,s}(r_{AS} - r) + k_{z,s}d + mod(r_{AS} - r - d\cot\theta, 2d\cot\theta) \cdot (\angle R_1 + \angle R_2), \tag{6}$$

where the first and second term refer to the propagation phase of polaritons. The third term refers to the phase accumulation due to the reflection from the top and bottom surface, which should also consider a reflection phase shift at the substrate, since what is measured is the polariton distribution at the top. Considering the quantized model of the polariton waveguide in Eq. 4 and the dispersion relation in Eq. 5, we could further simplify this expression as

$$\varphi(r,\phi) = k_{t,s}\left(r_{AS} - r + \frac{\delta_r}{2}\right) + s'2\pi. \tag{7}$$

If we design the Archimedean spiral such that $k_{t,s}\left(r_{AS} - r + \frac{\delta_r}{2}\right) = 2\pi l$, the phase accumulation of one Archimedean spiral is $(l + s')2\pi$. Therefore, the propagation phase accumulation after a rotation from $\phi = 0$ to $\phi = 2\pi$ is

$$\varphi_{PP} = (l + s') \cdot m2\pi \tag{8}$$

Here, we focus on the $s' = 0$ mode, which is also more easily excited because it has smaller momentum mismatch with free-space plane waves. Under a circularly polarized plane wave excitation, due the spin–orbit interactions in the near-field, we have the total phase accumulation

$$\varphi_{PP} = (l + s') \cdot m2\pi + \sigma 2\pi \tag{9}$$

which yields the total topological charge

$$L = (l + s') \cdot m + \sigma \tag{10}$$

where $s' = 0$ is the dominant mode. For left-handed structures, $\sigma = +1$ or -1 for left-handed circularly polarized (LCP) or right-handed circularly polarized (RCP) light, respectively.

We performed full-wave numerical simulations using the finite-difference time-domain commercially-available software Lumerical FDTD (https://www.lumerical.com/products/fdtd/). Two orthogonal linearly polarized waves with phase difference $\pm\pi/2$ were used to generate the circularly polarized excitation. An incident angle

of 10°, which is chosen for achieving the best agreement between experimental results and simulations, is applied because an off-axis parabolic mirror is used to focus the beam on the samples in the experiments. A monitor was placed at 20 nm above the top surface to calculate the near-field images.

Supplementary Information

The online version contains supplementary material available at https://doi.org/10.1186/s43593-022-00018-y.

Additional file 1: Figure S1. Schematic illustration of the isofrequency contour for type II hyperbolic materials and cross-section view of the sample. **Figure S2.** Experimental results for 295 nm hBN flake covering Au disks with $m = 4$. **Figure S3.** Experimental results for 170 nm hBN flake covering Au disks with $m = 2$. **Figure S4.** Optical microscope images of hBN flakes. **Figure S5.** Setup to verify the preservation of circular polarization after a parabolic mirror. **Table S1.** Output power vs degree of linear polarizer for the setup in Figure S5a. **Table S2.** Output power vs degree of linear polarizer for the setup in Figure S5b. **Figure S6.** Near-field amplitude images at 1590.5 cm^{-1}. **Figure S7.** Simulation and experimental results for an hBN flake excited through an Au disk without spiral arms. **Figure S8.** Simulation and experimental results for an hBN flake excited through Au spiral disks with $m = 1, 2,$ and 4 under linearly polarized light.

Availability of data and materials
All data are available upon request to the corresponding author.

Declarations

Ethics approval and consent to participate
Not applicable.

Consent for publication
Not applicable.

Competing interests
Cheng-Wei Qiu is an Editor for the journal, no other author has reported any competing interest.

Author details

[1]Photonics Initiative, Advanced Science Research Center, City University of New York, New York City, NY 10031, USA. [2]Department of Electrical and Computer Engineering, National University of Singapore, Singapore 116083, Singapore. [3]Department of Physics and Astronomy, The University of Georgia, Athens, GA 30602, USA. [4]Research Center for Functional Materials, National Institute for Materials Science, Tsukuba, Ibaraki 305-0044, Japan. [5]International Center for Materials Nanoarchitectonics, National Institute for Materials Science, Tsukuba, Ibaraki 305-0044, Japan. [6]Physics Program, Graduate Center, City University of New York, New York, NY 10016, USA.

References

1. J.D. Caldwell, I. Aharonovich, G. Cassabois, J.H. Edgar, B. Gil, D.N. Basov, Photonics with hexagonal boron nitride. Nat. Rev. Mater. **4**, 552–567 (2019)
2. F. Xia, H. Wang, D. Xiao, M. Dubey, A. Ramasubramaniam, Two-dimensional material nanophotonics. Nat. Photonics **8**, 899–907 (2014)
3. K.S. Novoselov, A. Mishchenko, A. Carvalho, A.H. CastroNeto, 2D materials and van der Waals heterostructures. Science (2016). https://doi.org/10.1126/science.aac9439
4. M. Wang, A. Krasnok, T. Zhang, L. Scarabelli, H. Liu, Z. Wu, L.M. Liz-Marzán, M. Terrones, A. Alù, Y. Zheng, Tunable fano resonance and plasmon-exciton coupling in single au nanotriangles on monolayer WS2 at room temperature. Adv. Mater. **30**, 1–8 (2018)
5. S. Lepeshov, M. Wang, A. Krasnok, O. Kotov, T. Zhang, H. Liu, T. Jiang, B. Korgel, M. Terrones, Y. Zheng, A. Alú, Tunable resonance coupling in single si nanoparticle-monolayer WS2 structures. ACS Appl. Mater. Interfaces **10**, 16690–16697 (2018)
6. D.N. Basov, M.M. Fogler, F.J. García De Abajo, Polaritons in van der Waals materials. Science (2016). https://doi.org/10.1126/science.aag1992
7. T. Low, A. Chaves, J.D. Caldwell, A. Kumar, N.X. Fang, P. Avouris, T.F. Heinz, F. Guinea, L. Martin-Moreno, F. Koppens, Polaritons in layered two-dimensional materials. Nat. Mater. **16**, 182–194 (2017)
8. Z. Dai, G. Hu, Q. Ou, L. Zhang, F. Xia, F.J. Garcia-Vidal, C.W. Qiu, Q. Bao, Artificial metaphotonics born naturally in two dimensions. Chem. Rev. **120**, 6197–6246 (2020)
9. A. Poddubny, I. Iorsh, P. Belov, Y. Kivshar, Hyperbolic Metamaterials. Nat. Photonics **7**, 958–967 (2013)
10. D. Correas-Serrano, J.S. Gomez-Diaz, M. Tymchenko, A. Alù, Nonlocal response of hyperbolic metasurfaces. Opt. Express **23**, 29434–29448 (2015)
11. G. Hu, J. Shen, C.W. Qiu, A. Alù, S. Dai, Phonon Polaritons and Hyperbolic Response in van der Waals Materials. Adv. Opt. Mater. **8**, 1–19 (2020)
12. J.D. Caldwell, A.V. Kretinin, Y. Chen, V. Giannini, M.M. Fogler, Y. Francescato, C.T. Ellis, J.G. Tischler, C.R. Woods, A.J. Giles, M. Hong, K. Watanabe, T. Taniguchi, S.A. Maier, K.S. Novoselov, Sub-diffractional volume-confined polaritons in the natural hyperbolic material hexagonal boron nitride. Nat. Commun. **5**, 1–9 (2014)
13. S. Dai, Z. Fei, Q. Ma, A.S. Rodin, M. Wagner, A.S. McLeod, M.K. Liu, W. Gannett, W. Regan, K. Watanabe, T. Taniguchi, M. Thiemens, G. Dominguez, A.H. CastroNeto, A. Zettl, F. Keilmann, P. Jarillo-Herrero, M.M. Fogler, D.N. Basov, Tunable phonon polaritons in atomically thin van der Waals crystals of boron nitride. Science **343**, 1125–1129 (2014)
14. P. Li, M. Lewin, A.V. Kretinin, J.D. Caldwell, K.S. Novoselov, T. Taniguchi, K. Watanabe, F. Gaussmann, T. Taubner, Hyperbolic phonon-polaritons in boron nitride for near-field optical imaging and focusing. Nat. Commun. **6**, 7507 (2015)
15. S. Dai, Q. Ma, T. Andersen, A.S. McLeod, Z. Fei, M.K. Liu, M. Wagner, K. Watanabe, T. Taniguchi, M. Thiemens, F. Keilmann, P. Jarillo-Herrero, M.M. Fogler, D.N. Basov, Subdiffractional focusing and guiding of polaritonic rays in a natural hyperbolic material. Nat. Commun. **6**, 1–7 (2015)
16. P. Li, I. Dolado, F.J. Alfaro-Mozaz, F. Casanova, L.E. Hueso, S. Liu, J.H. Edgar, A.Y. Nikitin, S. Vélez, R. Hillenbrand, Infrared hyperbolic metasurface based on nanostructured van der Waals materials. Science **359**, 892–896 (2018)
17. P. Li, G. Hu, I. Dolado, M. Tymchenko, C.W. Qiu, F.J. Alfaro-Mozaz, F. Casanova, L.E. Hueso, S. Liu, J.H. Edgar, S. Vélez, A. Alù, R. Hillenbrand, Collective near-field coupling and nonlocal phenomena in infrared-phononic metasurfaces for nano-light canalization. Nat. Commun. **11**, 1–8 (2020)
18. W. Ma, P. Alonso-González, S. Li, A.Y. Nikitin, J. Yuan, J. Martín-Sánchez, J. Taboada-Gutiérrez, P. Li, S. Vélez, C. Tollan, Z. Dai, Y. Zhang, S. Sriram, K. Kalantar-Zadeh, S.T. Lee, R. Hillenbrand, Q. Bao, In-plane anisotropic and ultra-low-loss polaritons in a natural van der Waals crystal. Nature **562**, 557–562 (2018)
19. Z. Zheng, J. Chen, Y. Wang, X. Wang, X. Chen, P. Liu, J. Xu, W. Xie, H. Chen, S. Deng, N. Xu, Highly confined and tunable hyperbolic phonon polaritons in van der waals semiconducting transition metal oxides. Adv. Mater. (2018). https://doi.org/10.1002/adma.201705318
20. G. Hu, Q. Ou, G. Si, Y. Wu, J. Wu, Z. Dai, A. Krasnok, Y. Mazor, Q. Zhang, Q. Bao, C.W. Qiu, A. Alù, Topological polaritons and photonic magic angles in twisted α-MoO3 bilayers. Nature **582**, 209–213 (2020)
21. Z. Dai, G. Hu, G. Si, Q. Ou, Q. Zhang, S. Balendhran, F. Rahman, B.Y. Zhang, J.Z. Ou, G. Li, A. Alù, C.W. Qiu, Q. Bao, Edge-oriented and steerable hyperbolic polaritons in anisotropic van der Waals nanocavities. Nat. Commun. **11**, 1–8 (2020)
22. J. Duan, N. Capote-Robayna, J. Taboada-Gutiérrez, G. Álvarez-Pérez, I. Prieto, J. Martín-Sánchez, A.Y. Nikitin, P. Alonso-González, Twisted nano-optics: manipulating light at the nanoscale with twisted phonon polaritonic slabs. Nano Lett. **20**, 5323–5329 (2020)
23. Z. Zheng, F. Sun, W. Huang, J. Jiang, R. Zhan, Y. Ke, H. Chen, S. Deng, Phonon Polaritons in Twisted Double-Layers of Hyperbolic van der Waals Crystals. Nano Lett. **20**, 5301–5308 (2020)
24. M. Autore, P. Li, I. Dolado, F.J. Alfaro-Mozaz, R. Esteban, A. Atxabal, F. Casanova, L.E. Hueso, P. Alonso-González, J. Aizpurua, A.Y. Nikitin, S. Vélez, R. Hillenbrand, Boron nitride nanoresonators for Phonon-Enhanced molecular vibrational spectroscopy at the strong coupling limit. Light Sci. Appl. **7**, 17172–17178 (2018)
25. A. Bylinkin, M. Schnell, M. Autore, F. Calavalle, P. Li, J. Taboada-Gutièrrez, S. Liu, J.H. Edgar, F. Casanova, L.E. Hueso, P. Alonso-Gonzalez, A.Y. Nikitin, R. Hillenbrand, Real-space observation of vibrational strong coupling between propagating phonon polaritons and organic molecules. Nat. Photonics **15**, 197–202 (2021)
26. K. Chaudhary, M. Tamagnone, X. Yin, C.M. Spägele, S.L. Oscurato, J. Li, C. Persch, R. Li, N.A. Rubin, L.A. Jauregui, K. Watanabe, T. Taniguchi, P. Kim, M. Wuttig, J.H. Edgar, A. Ambrosio, F. Capasso, Polariton nanophotonics using phase-change materials. Nat. Commun. **10**, 1–6 (2019)
27. J. Taboada-Gutiérrez, G. Álvarez-Pérez, J. Duan, W. Ma, K. Crowley, I. Prieto, A. Bylinkin, M. Autore, H. Volkova, K. Kimura, T. Kimura, M.H. Berger, S. Li, Q. Bao, X.P.A. Gao, I. Errea, A.Y. Nikitin, R. Hillenbrand, J. Martín-Sánchez, P. Alonso-González, Broad spectral tuning of ultra-low-loss polaritons in a van der Waals crystal by intercalation. Nat. Mater. **19**, 964–968 (2020)
28. D. Lee, S. So, G. Hu, M. Kim, T. Badloe, H. Cho, J. Kim, H. Kim, C.-W. Qiu, J. Rho, Hyperbolic metamaterials: fusing artificial structures to natural 2D materials. ELight **2**, 1–23 (2022)
29. H. Kim, J. Park, S.W. Cho, S.Y. Lee, M. Kang, B. Lee, Synthesis and dynamic switching of surface plasmon vortices with plasmonic vortex lens. Nano Lett. **10**, 529–536 (2010)
30. Y. Yang, L. Wu, Y. Liu, D. Xie, Z. Jin, J. Li, G. Hu, A.C.W. Qiu, Deuterogenic plasmonic vortices. Nano Lett. **20**, 6774–6779 (2020)
31. S.-W. Cho, J. Park, S.-Y. Lee, H. Kim, B. Lee, Coupling of spin and angular momentum of light in plasmonic vortex. Opt. Express **20**, 10083 (2012)
32. A. David, B. Gjonaj, G. Bartal, Two-dimensional optical nanovortices at visible light. Phys. Rev. B **93**, 1–5 (2016)
33. G. Spektor, A. David, G. Bartal, M. Orenstein, A. Hayat, Spin-patterned plasmonics: towards optical access to topological-insulator surface states. Opt. Express **23**, 32759 (2015)
34. C. Khandekar, Z. Jacob, Thermal spin photonics in the near-field of nonreciprocal media. New J. Phys. (2019). https://doi.org/10.1088/1367-2630/ab494d
35. Z. Jin, D. Janoschka, J. Deng, L. Ge, P. Dreher, B. Frank, G. Hu, J. Ni, Y. Yang, J. Li, C. Yu, D. Lei, G. Li, S. Xiao, S. Mei, H. Giessen, F.M. ZuHeringdorf, C.-W. Qiu, Phyllotaxis-inspired nanosieves with multiplexed orbital angular momentum. ELight **1**, 1–11 (2021)
36. Z. Ji, W. Liu, S. Krylyuk, X. Fan, Z. Zhang, A. Pan, L. Feng, A. Davydov, R. Agarwal, Photocurrent detection of the orbital angular momentum of light. Science (80-). **368**, 763–767 (2020)
37. K.Y. Bliokh, F.J. Rodríguez-Fortuño, F. Nori, A.V. Zayats, Spin-orbit interactions of light. Nat. Photonics **9**, 796–808 (2015)

38. S. Tsesses, K. Cohen, E. Ostrovsky, B. Gjonaj, G. Bartal, Spin-orbit interaction of light in plasmonic lattices. Nano Lett. **19**, 4010–4016 (2019)

39. J. Lin, J.P.B. Mueller, Q. Wang, G. Yuan, N. Antoniou, X.C. Yuan, F. Capasso, Polarization-controlled tunable directional coupling of surface plasmon polaritons. Science (80-). **340**, 331–334 (2013)

40. G. Spektor, E. Prinz, M. Hartelt, A.K. Mahro, M. Aeschlimann, M. Orenstein, Orbital angular momentum multiplication in plasmonic vortex cavities. Sci. Adv. **7**, 1–7 (2021)

41. K. Frischwasser, K. Cohen, J. Kher-Alden, S. Dolev, S. Tsesses, G. Bartal, Real-time sub-wavelength imaging of surface waves with nonlinear near-field optical microscopy. Nat. Photonics **15**, 442–448 (2021)

42. M. Schnell, P. Alonso-González, L. Arzubiaga, F. Casanova, L.E. Hueso, A. Chuvilin, R. Hillenbrand, Nanofocusing of mid-infrared energy with tapered transmission lines. Nat. Photonics **5**, 283–287 (2011)

43. M. Schnell, P. Sarriugarte, T. Neuman, A.B. Khanikaev, G. Shvets, J. Aizpurua, R. Hillenbrand, Real-space mapping of the chiral near-field distributions in spiral antennas and planar metasurfaces. Nano Lett. **16**, 663–670 (2016)

44. Z. Shen, Z.J. Hu, G.H. Yuan, C.J. Min, H. Fang, X.-C. Yuan, Visualizing orbital angular momentum of plasmonic vortices. Opt. Lett. **37**, 4627 (2012)

45. R.C. Devlin, A. Ambrosio, N.A. Rubin, J.P. Balthasar Mueller, F. Capasso, Arbitrary spin-to–orbital angular momentum conversion of light. Science **358**, 896–901 (2017)

46. R.C. Devlin, M. Khorasaninejad, W.T. Chen, J. Oh, F. Capasso, Broadband high-efficiency dielectric metasurfaces for the visible spectrum. Proc. Natl. Acad. Sci. **113**, 10473–10478 (2016)

47. Y. Gorodetski, A. Niv, V. Kleiner, E. Hasman, Observation of the spin-based plasmonic effect in nanoscale structures. Phys. Rev. Lett. **101**, 1–4 (2008)

48. L. Marrucci, C. Manzo, D. Paparo, Optical spin-to-orbital angular momentum conversion in inhomogeneous anisotropic media. Phys. Rev. Lett. **96**, 163905 (2006)

49. Y. Zhang, X. Yang, J. Gao, Orbital angular momentum transformation of optical vortex with aluminum metasurfaces. Sci. Rep. **9**, 1–9 (2019)

50. M.S. Soskin, V.N. Gorshkov, M.V. Vasnetsov, J.T. Malos, N.R. Heckenberg, Topological charge and angular momentum of light beams carrying optical vortices. Phys. Rev. A **56**, 4064–4075 (1997)

51. L. Xiong, Y. Li, D. Halbertal, M. Sammon, Z. Sun, S. Liu, J.H. Edgar, T. Low, M.M. Fogler, C.R. Dean, A.J. Millis, D.N. Basov, Polaritonic vortices with a half-integer charge. Nano Lett. **21**, 9256–9261 (2021)

52. Y. Dai, Z. Zhou, A. Ghosh, R.S.K. Mong, A. Kubo, C. BinHuang, H. Petek, Plasmonic topological quasiparticle on the nanometre and femtosecond scales. Nature **588**, 616–619 (2020)

53. L.P. Yang, Z. Jacob, Non-classical photonic spin texture of quantum structured light. Commun. Phys. (2021). https://doi.org/10.1038/s42005-021-00726-w

Publisher's Note

Springer Nature remains neutral with regard to jurisdictional claims in published maps and institutional affiliations.